molecular pharmaceutics

pubs.acs.org/molecularpharmaceutics

Article

Multinuclear Solid-State NMR and NMR Crystallography of Solid Forms of Creatine and Creatinine

Carl H. Fleischer, III, Victoria K. Rash, Zach T. Dowdell, Sara Termos, Xinsong Lin, Shubha S. Gunaga, Frédéric Mentink-Vigier, Juan Jimenez, A. M. Milinda Abeykoon, Sanjaya Senanayake, Sean T. Holmes,* and Robert W. Schurko

Cite This: *Mol. Pharmaceutics* 2026, 23, 3397−3409

Read Online

ACCESS | Metrics & More | Article Recommendations | Supporting Information

ABSTRACT: Creatine is a performance-enhancing supplement with two widely available commercial solid forms, namely, creatine monohydrate (creatine·H_2O) and creatine HCl, the latter of which does not have a reported crystal structure. Moreover, commercial formulations of creatine may contain creatinine, an undesired impurity phase resulting from the self-cyclization of creatine during manufacturing. Therefore, reliable methods for characterizing the different solid forms of creatine and detecting the presence of creatinine are essential. Herein, we address these challenges using ^{13}C, ^{15}N, and ^{35}Cl solid-state NMR (SSNMR) spectroscopy to obtain distinct spectral fingerprints for creatine·H_2O and creatine HCl, along with creatinine and creatinine HCl. The acquisition of these SSNMR spectra offers a robust approach for both the rapid characterization of each solid form and the detection of the impurity phases. Additionally, quadrupolar NMR crystallography-guided crystal structure prediction (QNMRX-CSP) was applied for the *de novo* crystal structure determination of creatine HCl, which was validated by the subsequently determined single-crystal X-ray diffraction (SCXRD) structure. Finally, to investigate the relationship between NMR parameters and structural features, ^{13}C and ^{15}N chemical shifts and ^{35}Cl electric field gradient (EFG) tensors were computed from geometry-optimized structures of the four solid forms by using dispersion-corrected DFT-D2* methods. This integrative approach offers a powerful framework for advancing the structural understanding and quality control of creatine-based supplements and next-generation formulations, as well as a wide range of other solid pharmaceuticals and nutraceuticals.

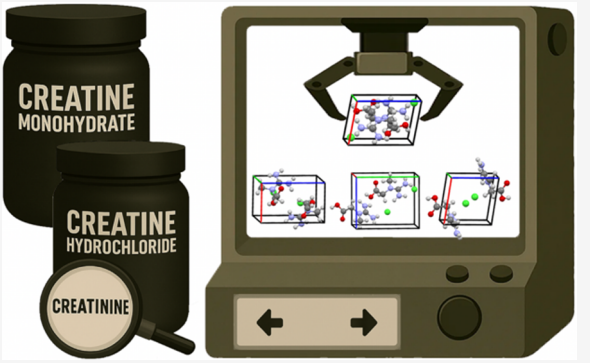

KEYWORDS: *NMR, NMR crystallography, crystal structure prediction, X-ray diffraction, structure determination*

1. INTRODUCTION

Creatine is an extensively researched performance-enhancing supplement as evidenced by a search using Clarivate Web of Science with the keywords "creatine" and "supplement," which resulted in approximately 4000 peer-reviewed articles. This interest in creatine is well merited, as creatine supplementation has been shown to provide many health benefits, including increased lean muscle mass, faster muscle recovery, greater muscle retention, and improved cognitive performance.[1−3] These benefits, as well as many others, have influenced many people to take it daily. Among its various solid forms, creatine monohydrate (creatine·H_2O) is the typical form consumed during supplementation; however, because of its low solubility in water, there has been considerable effort in developing formulations with a more favorable solubility profile. This search has resulted in the development of over 80 solid forms of creatine,[4] of which there are relatively few with known crystal structures, including solid forms available for commercial purchase (e.g., creatine HCl). Hence, to better understand the relationships between the different solid forms of creatine, including its salts and solvates, and the enhancement of physicochemical properties such as solubility, stability, and bioavailability, comprehensive structural screening is essential.

The industrial synthesis of the many solid forms of creatine typically begins with the production of creatine·H_2O, where large reactors containing sarcosine and cyanamide in an aqueous medium are heated to induce a condensation reaction.[5] Under these conditions, creatine can undergo self-cyclization to form creatinine, an undesired impurity phase.[4−7] While the potential clinical applications of creatinine are developing,[8,9] it is more commonly considered a waste

Received: January 19, 2026
Revised: April 22, 2026
Accepted: April 23, 2026
Published: May 7, 2026

product, filtered from the bloodstream by the kidneys and excreted through urination.[10,11] In fact, monitoring of creatinine levels is used to evaluate kidney function, where elevated levels of creatinine in the bloodstream may indicate health issues.[12] Therefore, reliable methods for detecting creatinine in different forms of creatine are necessary to ensure product purity, minimize unnecessary kidney stress, and avoid false positives that erroneously suggest kidney dysfunction.

Solid-state NMR (SSNMR) spectroscopy is a valuable method for providing distinct spectral fingerprints of the different solid forms of creatine and creatinine, enabling both the detection of impurity phases and the identification of new solid forms. Additionally, it is possible to use NMR crystallography (NMRX), which combines information from SSNMR spectroscopy, X-ray diffraction (typically powder X-ray diffraction, PXRD), and quantum chemical calculations, to refine, validate, and determine crystal structures of these solid forms, especially in cases where crystals suitable for single-crystal XRD (SCXRD) are unavailable.[13−17] Recently, our group designed an NMRX protocol called *quadrupolar NMR crystallography-guided crystal structure prediction* (QNMRX-CSP).[18−21] Early applications of QNMRX-CSP have relied on experimental data from PXRD and ^{35}Cl SSNMR (which is ideal for the study of HCl salts of active pharmaceutical ingredients, nutraceuticals, and other organic compounds, due to the sensitivity of ^{35}Cl electric field gradient (EFG) tensors to the local hydrogen bonding environments of chloride ions)[22−27] and employed Monte Carlo simulated annealing (MC-SA)[28] and dispersion-corrected density functional theory (DFT-D2*)[29] calculations for the generation of candidate structures, refinement of atomic coordinates, and calculation of NMR interaction tensors. The strategic combination of these data and methods allows for the *de novo* structural determination of organic HCl salts.

Herein, we present a study describing the use of multinuclear SSNMR to characterize several forms of creatine and creatinine (Scheme 1), including creatine monohydrate (**Crea·H_2O**), creatine HCl (**CreaHCl**), creatinine (**CreaT**), and creatinine HCl (**CreaTHCl**). These solid forms of creatine and creatinine were selected due to their widespread commercial availability and the likelihood that the solid forms of creatinine may occur as impurity phases in their respective commercial products (i.e., **CreaT** in **Crea·H_2O** and **CreaTHCl** in **CreaHCl**). Additionally, we demonstrate the use of QNMRX-CSP for the *de novo* structural determination of **CreaHCl**, making a first step toward resolving one of the many previously unknown crystal structures among the over 80 solid forms of creatine (we note that the crystal structures of the other three solid forms have been reported previously).[30−32] Since QNMRX-CSP is still a nascent technique, the SCXRD structure of **CreaHCl** was subsequently determined in order to aid with structural validation. Finally, the *de novo* structural determination of **CreaHCl** allows for the investigation of the relationship between NMR parameters and structural features of the four solid forms, where ^{13}C and ^{15}N chemical shifts and ^{35}Cl EFG tensors were computed from DFT-D2* geometry-optimized structural models. This work highlights the potential of QNMRX-CSP as a powerful method for the *de novo* structural determination of organic HCl salts with broader applications to other pharmaceutical and nutraceutical compounds.

Scheme 1. Molecular Diagrams for (A) Crea·H_2O, (B) CreaT, (C) CreaHCl, and (D) CreaTHCl, with Numbers Labeled for Carbon and Nitrogen Atoms for Reference to Tables 2,3

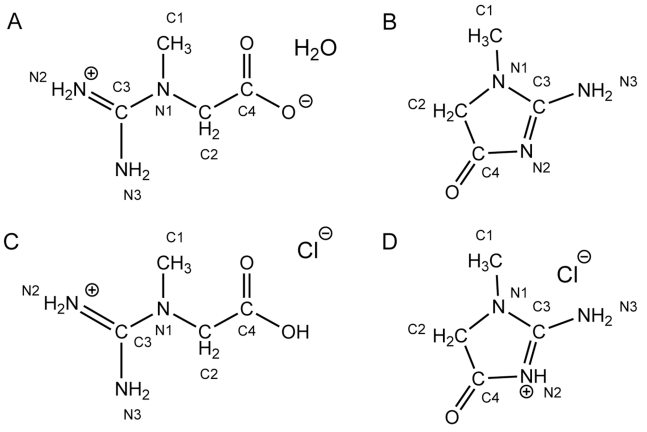

2. METHODS

2.1. Materials

Crea·H_2O, **CreaT**, and **CreaTHCl** were purchased from Sigma-Aldrich and used without further purification. **CreaHCl** from Beyond Raw Chemistry Laboratories was purchased from a local supplement store and used without further purification. PXRD was used to confirm the identities of **Crea·H_2O**, **CreaT**, and **CreaTHCl** via comparison to the simulated PXRD patterns (*vide infra*).

2.2. X-ray Diffraction

2.2.1. Room Temperature Powder X-ray Diffraction. PXRD patterns were acquired at room temperature using a Rigaku SmartLab X-ray diffractometer featuring a Cu *Kα* radiation source and a D/tex Ultra 250 1D silicon strip detector. The voltage and amperage of the X-ray tube were set to 40 kV and 15 mA, respectively. The PXRD patterns were acquired by scanning 2*θ* from 5 to 50° with step sizes of 0.01° and at a rate of 0.5° min^{-1}.

The room temperature PXRD pattern of **CreaHCl** was smoothed using a width of 0.01°, background-corrected, and indexed using the X-Cell scheme in the Reflex Powder Index module in BIOVIA Materials Studio 2020.[33] The peak positions of this PXRD pattern were determined using the simple detection method in the Reflex Powder Index module starting from 2*θ* = 5° and including up to 28 peaks with a low amplitude cutoff of 5.0%.

2.2.2. Synchrotron Powder X-ray Diffraction. All samples were finely ground before loading them into 1 mm O.D. Kapton capillary tubes, which were sealed on both ends with a composite sealant. Synchrotron PXRD patterns were acquired at 100 K and carried out in capillary transmission geometry using a PerkinElmer amorphous silicon area detector placed *ca.* 1000 mm downstream of the samples at 28-ID-1 Pair Distribution Function beamline of the National Synchrotron Light Source II at Brookhaven National Laboratory. The NSLS-II beamline 28 features a synchrotron radiation source (*λ* = 0.1665 Å). The 2*θ* values for the synchrotron PXRD patterns were calibrated by using a Ni metal standard.

2.2.3. Single-Crystal X-ray Diffraction. A single crystal of **CreaHCl** was serendipitously found in the commercial sample. The single crystal was coated with perfluoroether oil and placed on a nylon loop inside an XtaLAB Synergy Dualflex HyPix four-circle diffractometer, which features a microfocus sealed X-ray tube, uses a mirror as a monochromator, and includes a HyPix detector. The diffractometer also features an Oxford Cryostream 800 low-temperature device and uses Cu *Kα* radiation. SCXRD data were collected at 297.15 K, and the structure was solved by SHELXT and by a full-matrix least-squares method against F^2 (Table S1).[34,35] All non-hydrogen atoms were refined with anisotropic displacement parameters. Hydrogen atoms were refined isotopically on calculated

https://doi.org/10.1021/acs.molpharmaceut.6c00077
Mol. Pharmaceutics 2026, 23, 3397−3409

positions using a riding model, with their U_{iso} values constrained to 1.5 times the U_{eq} of their pivot atoms for terminal sp^3 carbon atoms and 1.2 times those for all other atoms.

2.3. Solid-State NMR

Solid-state NMR (SSNMR) spectra were acquired at 14.1 T (two 14.1 T spectrometers were used, one for room temperature and the other for experiments at 100 K) and 18.8 T at the National High Magnetic Field Laboratory (NHMFL, Tallahassee, FL) with Bruker Avance NEO spectrometers and Oxford widebore magnets. The relevant Larmor frequencies for the (i) room temperature experiments at 14.1 T are $\nu_0(^1H)$ = 600.1 MHz, $\nu_0(^{13}C)$ = 150.89 MHz, $\nu_0(^2H)$ = 92.12 MHz, and $\nu_0(^{35}Cl)$ = 58.797 MHz; (ii) experiments conducted at 100 K are $\nu_0(^1H)$ = 600.49 MHz, and $\nu_0(^{15}N)$ = 60.85 MHz; and (iii) experiments carried out at 18.8 T are $\nu_0(^1H)$ = 799.74 MHz, and $\nu_0(^{35}Cl)$ = 78.358 MHz. Preliminary ^{13}C and ^{15}N dynamic nuclear polarization[36,37] cross-polarization/magic-angle spinning (CP/MAS) SSNMR spectra were acquired using the ramped-amplitude CP/MAS pulse sequence[38−42] at 100 K for samples impregnated with ca. 20 uL of 15 mM AsymPol-POK[43] in ethylene glycol (Figure S1). Comparison of the microwave "on" and "off" spectra indicated minimal signal enhancement in the former, perhaps due to the dissolution of the sample in the biradical matrix. As such, all $^1H\rightarrow^{15}N$ CP/MAS NMR spectra were acquired at 100 K to enhance the Boltzmann population difference and improve signal intensity. All other acquisition parameters are summarized in the Supporting Information (Tables S2−S4).

2.3.1. $^1H\rightarrow^{13}C\{^1H\}$ Experiments. $^1H\rightarrow^{13}C\{^1H\}$ cross-polarization/magic-angle spinning (CP/MAS) NMR spectra were acquired at 14.1 T at room temperature with a spinning rate of ν_{rot} = 10 kHz, using the $^1H\rightarrow^{13}C$ ramped-amplitude CP/MAS pulse sequence.[38−42] Spectra were acquired using ^1H $\pi/2$ pulses of 2.5 μs, contact times between 1 and 6 ms, recycle delays between 24 and 60 s, a 50 kHz ^1H and 42 kHz ^{13}C Hartmann−Hahn match, and SPINAL-64 ^1H decoupling (ν_2 = 100 kHz). The experiments used an NHMFL-built 3.2 mm low-E HXY MAS probe with samples packed in 3.2 mm o.d. zirconia rotors. ^{13}C chemical shifts were referenced to TMS ($\delta_{iso}(^{13}C)$ = 0 ppm) using the carboxyl peak of ^{13}C-labeled α-glycine at $\delta_{iso}(^{13}C)$ = 176.5 ppm as a secondary reference.[44]

2.3.2. $^1H\rightarrow^{15}N\{^1H\}$ Experiments. $^1H\rightarrow^{15}N\{^1H\}$ CP/MAS NMR spectra were acquired at a temperature of 100 K and ν_{rot} = 8 kHz at 14.1 T using the $^1H\rightarrow^{15}N$ ramped-amplitude CP/MAS pulse sequence. Spectra were acquired using ^1H $\pi/2$ pulses of 2.5 μs, contact times of both 200 μs and 5 ms (for the purpose of peak assignment, *vide infra*), recycle delays between 1.69 and 2.6 s, a 49 kHz ^1H and 44 kHz ^{15}N Hartman-Hahn match, and SPINAL-64 ^1H decoupling (ν_2 = 98 kHz). The experiments used an NHMFL-built 3.2 mm HXY MAS probe with samples packed in 3.2 mm sapphire rotors. ^{15}N chemical shifts were referenced to neat NH_3 ($\delta_{iso}(^{15}N)$ = 0 ppm) using NH_4Cl at $\delta_{iso}(^{15}N)$ = 37.6 ppm at 100 K as a secondary reference.[45]

2.3.3. $^{35}Cl\{^1H\}$ Experiments. The $^{35}Cl\{^1H\}$ SSNMR spectra were acquired at room temperature under static conditions at 14.1 and 18.8 T and under MAS at 18.8 T. Static spectra were acquired using the quadrupolar Carr-Purcell Meiboom-Gill (CPMG) pulse sequence[46] (the first echo was acquired as a full echo) and in an NHMFL-built 5 mm HX probe with samples packed into 5 mm o.d. sample holders. Direct-excitation MAS spectra were acquired using a rotor-synchronized Hahn-echo pulse sequence[47,48] at ν_{rot} = 15 kHz with a 3.2 mm low-E HXY MAS NHMFL-built probe with samples packed in 3.2 mm o.d. zirconia rotors. ^{35}Cl chemical shifts were referenced to 0.1 M NaCl (aq) at $\delta_{iso}(^{35}Cl)$ = 0.0 ppm using NaCl (s) at $\delta_{iso}(^{35}Cl)$ = −41.11 ppm as a secondary reference.[49] ^{35}Cl SSNMR parameters were obtained by simulating the experimental spectra using ssNake v1.4.[50] Uncertainties in the quadrupolar and chemical shift tensor parameters were estimated by spectral simulations, using the bidirectional variation of each parameter until the simulated powder pattern no longer matched the experimental spectra.

2.4. QNMRX-CSP

QNMRX-CSP[18,19] (Scheme S1), which relies on experimental inputs from indexed PXRD patterns (i.e., space group and unit cell parameters) and ^{35}Cl SSNMR spectra (i.e., ^{35}Cl EFG tensors), was used to determine the crystal structure of **CreaHCl**. QNMRX-CSP consists of three *modules*, each of which comprises steps that are used for predicting or refining candidate structures: (i) Module 1 (M1) develops "chemically sensible" molecular fragments (i.e., organic molecules and Cl^- ions); (ii) Module 2 (M2) uses MC-SA to predict the candidate structures; (iii) Module 3 (M3) employs a QNMRX routine, which consists of several rounds of plane-wave DFT-D2* geometry optimizations of candidate structures, as well as calculations of static lattice energies and ^{35}Cl EFG tensors. The candidate structures that emerge from the application of these three modules undergo structural validation (section 2.6).

M2 and M3 employ *metric sets* comprised of *metrics* (section 2.5; Table S5) that are strategically positioned to retain candidate structures that are most likely to be validated (section 2.6) as the correct crystal structure. The entire QNMRX-CSP protocol, along with the choices of metric sets, metrics, structural validation terms, and their respective thresholds, has been benchmarked previously.[18−21]

Two graphical user interfaces are used for these applications: (i) BIOVIA Materials Studio 2020, which facilitates calculations in CASTEP 20.1 and Polymorph, and (ii) CASTEP Data Manager, an in-house-built program for the automation of CASTEP calculations and data management.

2.4.1. CASTEP. Plane-wave DFT-D2*[29] geometry optimizations and NMR tensor calculations were performed using CASTEP.[51] *Convergent geometry optimizations* and NMR tensor calculations used the RPBE functional,[52] zeroth-order regular approximation (ZORA)[53] scalar-relativistic ultrasoft pseudopotentials generated on-the-fly,[54] a plane-wave cutoff energy of 800 eV, and a *k*-point spacing of 0.05 $Å^{-1}$ using a grid generated via a Monkhorst−Pack algorithm.[55] Convergence is reached after a maximum energy change of 5×10^{-6} eV $atom^{-1}$, displacement of 5×10^{-4} Å, and a maximum force of 10^{-2} eV $Å^{-1}$. *Truncated geometry optimizations* use the above-mentioned parameters and set the maximum number of BFGS[56] cycles to 5.

^{13}C, ^{15}N, and ^{35}Cl isotropic magnetic shieldings were calculated using the gauge including projector augmented wave[57] (GIPAW) method, on DFT-D2* convergent geometry-optimized structural models. Magnetic shieldings were converted to the chemical shift scale using the least-squares linear regression based on additional calculations for three series of systems, one for each of the nuclides, previously characterized in other SSNMR studies. For ^{13}C chemical shifts, this was accomplished using geometry-optimized structural models of *L*-histidine $HCl{\cdot}H_2O$,[58] α-glycine,[59] γ-glycine,[60] and *L*-asparagine$\cdot H_2O$[61] (Figure S2).[62] ^{15}N magnetic shieldings were converted to chemical shifts using the geometry-optimized structural models of 15 organic crystals consisting of 35 ^{15}N chemical shifts (Table S6; Figure S2).[63−65] The calculated ^{35}Cl isotropic chemical shielding of a DFT-D2* geometry-optimized structural model of *L*-histidine $HCl{\cdot}H_2O$, σ_{iso} = 951.44 ppm, was referenced to δ_{iso} = 34.5 ppm on the chemical shift scale.[66]

Atomic Hirshfeld charges for use in M1 for **CreaHCl** were obtained from convergent geometry-optimized structural models from the known crystal structures of **Crea·H_2O**[30] and anhydrous creatine (Form II)[67] as starting points (Table S7). The average calculated Hirshfeld charges of the structural models of **Crea·H_2O** and anhydrous creatine (Form II) were applied to each atom in the structural model of **CreaHCl**, with the exception of a few H atoms, to which minor modifications to charges were made to ensure that the sum of all charges was equal to zero, as these sites have the largest variation in calculated charges. **Crea·H_2O** and anhydrous creatine both have deprotonated carboxylic acids and no Cl^- ion, so the Hirshfeld charges on the O and H atoms in the R−O−H moieties and Cl^- ion in **CreaHCl** were set to −0.140, 0.100, and −0.270, respectively.

https://doi.org/10.1021/acs.molpharmaceut.6c00077
Mol. Pharmaceutics 2026, 23, 3397−3409

2.4.2. Polymorph Software. Polymorph, which predicts candidate structures for **CreaHCl** in M2, relies on the determination of the space group (obtained from indexing the PXRD pattern of **CreaHCl**) and the development of molecular fragments (i.e., creatine cation and a Cl^- ion from M1, section 3.3). Polymorph uses a four-step routine to predict a maximum of 10,000 candidate structures per *trial*, which is one iteration of the four-step routine that is comprised of (i) packing, (ii) clustering, (iii) Dreiding force-field[68] geometry optimization, and (iv) clustering. During both packing and Dreiding force-field geometry optimization, the relative atomic coordinates of the atoms in the molecular fragments are restricted; however, the relative positions and orientations of the motion groups are allowed to vary. Packing employs an MC-SA[28] algorithm to generate the candidate structures, using a maximum and minimum temperature of 1.5×10^5 K and 300 K, respectively, heating and cooling factors of 0.025 and 0.0005, respectively, and a minimum move factor of 10^{-10}. Clustering removes duplicate structures based on a radial distribution cutoff of 7.0 Å, a tolerance of 0.13, and 140 bins, retaining the structure with the lowest static lattice energy. Dreiding force-field geometry optimizations are then employed, with structural convergence achieved after a maximum energy change of 2×10^{-5} kcal mol^{-1}, a maximum displacement of 10^{-5} Å, a maximum force of 10^{-3} kcal mol^{-1} $Å^{-1}$, and a maximum stress of 10^{-3} GPa. Another round of clustering is then employed to remove duplicated structures. After 10 trials of Polymorph are completed, the candidate structures are clustered one more time to remove duplicate structures obtained from across all trials.

2.5. Metrics

QNMRX-CSP applies multiple metrics, such as unit cell parameters, static lattice energies, and ^{35}Cl EFG tensors, to retain the most plausible candidate structures of **CreaHCl**. These metrics are grouped into *metric sets*, which are strategic combinations applied simultaneously to retain structural models that are most likely to match the experimental structural data. The metrics in each metric set and their position within QNMRX-CSP are found in Table S5 and Scheme S1, respectively.

2.5.1. Unit Cell Parameters. Candidate structures are retained by comparing their unit cell parameters to those obtained from indexing the PXRD pattern of **CreaHCl**. Structures are retained if their unit cell parameters are within ± 20% of the indexed values.

2.5.2. Static Lattice Energies. Candidate structures are retained by calculating their static lattice energies (E_{lat}) and comparing them to the lowest overall static lattice energy (E_{low}) in M2 and M3. In M2, candidate structures are retained such that

$$E_{low} \leq E_{lat} \leq 0.865 \cdot E_{low} \quad (1)$$

In M3, candidate structures are retained after each round of DFT-D2* geometry optimization if their $\Delta E_{lat} = E_{lat} - E_{low}$ values are less than or equal to an energy threshold (E_{thresh}) such that

$$\Delta E_{lat} = E_{lat} - E_{low} \leq E_{thresh} \quad (2)$$

The value of E_{thresh} ranges from 135 to 1 kJ mol^{-1}, depending on the metric set in which it is used (see Table S5).

2.5.3. ^{35}Cl EFG Distance. Candidate structures are retained based on the similarity between experimental and calculated ^{35}Cl EFG tensors, as evaluated using the EFG distance (Γ_{EFG}), which is reminiscent to the chemical shift distance by Alderman et al.[29,69]

$$\Gamma_{EFG} = \left(\frac{1}{15}[3\Delta_{11}^2 + 3\Delta_{22}^2 + 3\Delta_{33}^2 + 2\Delta_{11}\Delta_{22} + 2\Delta_{22}\Delta_{33} + 2\Delta_{11}\Delta_{33}]\right)^{1/2} \quad (3)$$

$$\Delta_{kk} = |V_{kk}^{calc} - V_{kk}^{exp}| \quad (4)$$

Γ_{EFG} uses ^{35}Cl EFG tensor principal components V_{kk}, where k = 1, 2, and 3, to assess the degree of similarity between the experimental and calculated ^{35}Cl EFG tensors using a scalar value. This equation assumes that the two ^{35}Cl EFG tensors are coincident. A value of Γ_{EFG} = 0 indicates that the EFG tensors are identical. Benchmarking QNMRX-CSP studies have determined that an $\Gamma_{EFG} \leq 0.49$ MHz calculated using the experimental and calculated ^{35}Cl EFG tensors on a DFT-D2* refined structural model indicates a good structural match.[18,19]

2.6. Structural Validation Terms

QNMRX-CSP validates the final candidate structural models of **CreaHCl** using the *R*-factor (R) and an atomic position RMSD (Δ_{RMSD}^{AP}). These comparisons are made using the simulated PXRD patterns and atomic positions determined from the QNMRX-CSP and SCXRD structural models, where a good structural match is met when $R \leq 10\%$[70−72] and $\Delta_{RMSD}^{AP} \leq 0.2$ Å.[72,73] Additionally, qualitative comparisons are made using visual comparisons of the experimental PXRD patterns to those obtained from simulations as well as comparisons of the packing motifs in the SCXRD and QNMRX-CSP structural models. Although *R*-factors are also inspected qualitatively, the candidate structural models from QNMRX-CSP are not refined against the experimental PXRD data; consequently, their *R*-factors can be significantly higher than those typically reported for refined structures in the Cambridge Structural Database (i.e., $R \geq 10\%$).[72,73]

2.6.1. *R*-Factor. PXRD patterns were simulated in the Powder Pattern tool in Mercury 2024.3.1 with a Cu $K\alpha_1$ (λ = 1.54056 nm) and a Cu $K\alpha_2$ radiation source (λ = 1.54439 nm). The 2θ values ranged from 5 to 50° in step sizes of 0.01° with a full-width half-height peak width of 0.07°. *R*-factors were computed by the following expression

$$R = \frac{\sum |(|F_0| - |F_c|)|}{\sum |F_0|} \times 100\% \quad (5)$$

where F_0 and F_c are the calculated structure factor amplitudes of the reference and candidate structures, respectively, summed over all reflections.

2.6.2. Atomic Position RMSDs. Δ_{RMSD}^{AP} values were calculated using the CSD-Materials Crystal Packing Similarity in Mercury 2024.3.1, employing a 15-molecule cluster with a distance and angle tolerance of 20% and 20°, respectively.

3. RESULTS AND DISCUSSION

Herein, several methods for characterizing **Crea·H_2O**, **CreaT**, **CreaHCl**, and **CreaTHCl** (Scheme 1) are discussed, including PXRD (section 3.1), SSNMR (section 3.2), QNMRX-CSP (section 3.3), SCXRD (section 3.4), and NMR tensor calculations using DFT (section 3.5). PXRD was used for phase identification, detection of impurities, and indexing of the unit cell of **CreaHCl**. ^{13}C, ^{15}N, and ^{35}Cl SSNMR spectra afford insights into local atomic environments, provide spectral fingerprints, and aid in identifying small-weight-percent impurities. QNMRX-CSP was used for the *de novo* structural determination of **CreaHCl** using data acquired from PXRD and ^{35}Cl SSNMR. SCXRD was used to validate the structural models of **CreaHCl** that were determined from QNMRX-CSP (*N.B.*: SCXRD analysis was performed only after QNMRX-CSP had produced structural models with data that matched well with that from the experimental PXRD and ^{35}Cl SSNMR). Finally, DFT-D2* geometry optimizations were performed on structural models based on the crystal structures of different solid forms of creatine and creatinine, along with subsequent calculations of NMR interaction tensors, which are correlated to structural features.

3.1. Powder X-ray Diffraction

PXRD provides fingerprints for all solid forms of creatine and creatinine, with variable temperature PXRD allowing for the observation of phase changes. However, small-weight-percent impurities are sometimes not detectable. The room temperature and 100 K synchrotron PXRD patterns of **Crea·H_2O**

https://doi.org/10.1021/acs.molpharmaceut.6c00077
Mol. Pharmaceutics 2026, 23, 3397−3409

Table 1. Crystallographic Information for the Solid Forms of Creatine and Creatinine[a]

	CCDC code	temperature (K)	space group	a (Å)	b (Å)	c (Å)	β (°)
Crea·H_2O	CREATH06	295	$P2_1/a$	12.159(1)	5.038(2)	12.491(2)	108.87(1)
CreaT	CREATI02	295	$P2_1/n$	8.015(1)	5.926(1)	11.419(1)	96.25(1)
CreaHCl	this work[b]	298(3)	$P2_1$	5.0929(542)	10.7395(632)	7.3219(269)	100.9710(5572)
CreaHCl	this work[c]	297.15	$P2_1$	5.09231(9)	10.7393(2)	7.32529(15)	100.9606(18)
CreaTHCl	XEBJUL	120	$P2_1/n$	8.462(1)	7.707(1)	10.222(1)	98.37(1)

[a]Values in parentheses denote the uncertainty in the last digit(s) of the experimental value. [b]The space group and unit cell parameters of **CreaHCl** were determined from indexing the PXRD pattern of **CreaHCl**. [c]The space group and unit cell parameters of **CreaHCl** were determined from the SCXRD data.

match well with the simulated patterns derived from the previously reported crystal structure (Figures S3 and S4).[30] For **CreaT**, the 100 K synchrotron PXRD pattern matches well with the simulated pattern derived from its previously reported crystal structure;[32] however, the room temperature PXRD pattern shows significant intensity differences. These differences are attributed to preferred orientation effects, likely arising from insufficient sample grinding, and when accounted for, the simulated PXRD pattern matches well. For **CreaTHCl**, no room temperature SCXRD structure has been reported; therefore, the simulated PXRD pattern of the SCXRD structure determined at 120 K was used for comparisons, which accounts for the slight differences in the peak positions.[31] These comparisons for **Crea·H_2O**, **CreaT**, and **CreaTHCl** show no signs of any impurity phase(s). Since there is no reported crystal structure for **CreaHCl**, the room temperature PXRD pattern was acquired (Figure S3) for determining its space group and unit cell parameters. This PXRD pattern features peak broadening and doubling, which becomes apparent at 2θ *ca.* 24.5° and higher. The broadened and doubled peaks consist of two closely spaced peaks, a more intense major peak, and a less intense minor peak. Of the two, the minor peak is consistently shifted to higher 2θ values with respect to the major peak. The integrated intensity of the minor peak is *ca.* 1/2 that of the major peak. These features are characteristic of a Cu $K\alpha$ doublet, corresponding to Cu $K\alpha_1$ (λ = 1.54056 nm) and Cu $K\alpha_2$ (λ = 1.54439 nm). Therefore, an accurate space group and unit cell parameters of **CreaHCl** were determined by indexing only the Cu $K\alpha_1$ peaks (Table 1, see also section 3.3).

3.2. Solid-State NMR Spectroscopy

Below, we present the ^{13}C, ^{15}N, and ^{35}Cl SSNMR data for the solid forms of creatine and creatinine. A detailed discussion of the spectra, including peak assignments and structural interpretations from NMR tensor interaction calculations, is provided in section 3.5.

3.2.1. ^{1}H→^{13}C CP/MAS SSNMR. ^{1}H→^{13}C CP/MAS SSNMR spectra (Figure 1) each have four peaks, indicating four chemically and crystallographically distinct carbon sites in the asymmetric unit of each solid form (i.e., Z' = 1). This is consistent with the three known crystal structures and provides useful information for the structural determination of **CreaHCl**. Peak assignments were made using GIPAW calculations (Table 2, see also section 3.5). The **CreaHCl** spectrum (Figure 1C) features an additional peak at 34.4 ppm that matches that of the C1 carbon (N−CH_3 moiety) peak of **CreaTHCl** (underlying red spectrum). However, it is difficult to confirm the impurity as **CreaTHCl**, given the absence of other peaks attributable to this phase, largely due to potential overlaps with intense peaks arising from **CreaHCl** (also *vide infra*).

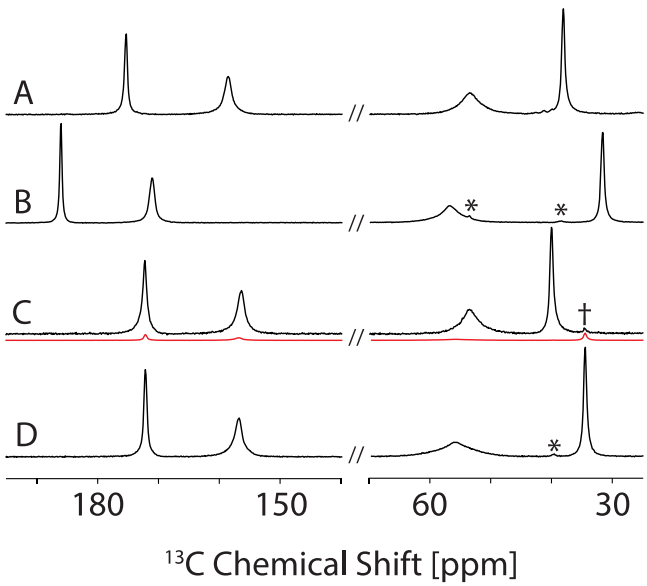

Figure 1. ^{1}H→^{13}C CP/MAS spectra of (A) **Crea·H_2O**, (B) **CreaT**, (C) **CreaHCl**, and (D) **CreaTHCl** acquired at 14.1 T, room temperature, and ν_{rot} = 10 kHz. The red spectrum underneath the **CreaHCl** spectrum corresponds to the **CreaTHCl** spectrum that has been scaled down to match the peak intensity at *ca.* 34.5 ppm. The asterisks denote the spinning side bands. The † indicates a peak corresponding to an impurity in the sample.

3.2.2. ^{1}H→^{15}N CP/MAS SSNMR. ^{1}H→^{15}N CP/MAS SSNMR spectra were acquired at 100 K using short and long contact times of 200 μs and 5 ms, respectively (Figure 2). Each ^{15}N spectrum reveals three peaks, again consistent with Z' = 1 for the samples with known structures, as well as for **CreaHCl** (*vide supra*), and there are no additional peaks in the ^{15}N SSNMR spectrum of **CreaHCl** corresponding to **CreaTHCl**, indicating that the latter is not present in any significant amount. However, because **CreaT**, **CreaHCl**, and **CreaTHCl** do not have reported crystal structures at or below 100 K, a synchrotron PXRD pattern for each was acquired at 100 K (Figure S4), revealing that no phase changes occurred over this temperature range. GIPAW calculations of ^{15}N NMR tensors do not yield the best agreement with experiment, providing assignments of only some of the peaks (Table 3, see also section 3.5 for further discussion). As a result, variable-contact time CP/MAS SSNMR was used to complete most of the peak assignments. These spectra have substantial differences in peak intensities at two contact times of 200 μs and 5 ms for the nonprotonated N1 sites, $R_1R_2NCH_3$, in **Crea·H_2O**, **CreaHCl**, **CreaT**, and **CreaTHCl**, as well as the N2 site, R_1R_2N, of **CreaT**. The remaining peaks were assigned to the

https://doi.org/10.1021/acs.molpharmaceut.6c00077
Mol. Pharmaceutics 2026, 23, 3397−3409

Table 2. Experimental and Calculated ^{13}C Chemical Shifts[a]

		C1 (ppm)	C2 (ppm)	C3 (ppm)	C4 (ppm)	Δ^{CS}_{RMSD} (ppm)[b]
Crea·H$_2$O	exp.	38.0(7)	53.3(38)	158.7(14)	175.4(5)	
	calc.	34.4	53.3	152.5	176.4	3.59
CreaT	exp.	31.6(7)	56.7(32)	171.0(10)	186.0(4)	
	calc.	28.3	55.9	166.5	186.1	2.83
CreaHCl	exp.	39.9(7)	53.3(25)	156.4(13)	172.2(8)	
	calc.	36.0	53.9	150.8	175.1	3.72
CreaTHCl	exp.	34.4(6)	55.7(50)	156.7(17)	172.1(6)	
	calc.	31.3	56.3	153.2	174.5	2.64

[a]Atomic numbering scheme is provided in Scheme 1. [b]The agreement between calculated (δ_i^{calc}) and experimental (δ_i^{exp}) isotropic chemical shifts was compared using a chemical shift root-mean-square deviation (Δ^{CS}_{RMSD}): $\Delta^{CS}_{RMSD} = \sqrt{\frac{\sum_{i=1}^{N}(\delta_i^{calc} - \delta_i^{exp})^2}{N}}$ where N is the total number of isotropic chemical shifts.

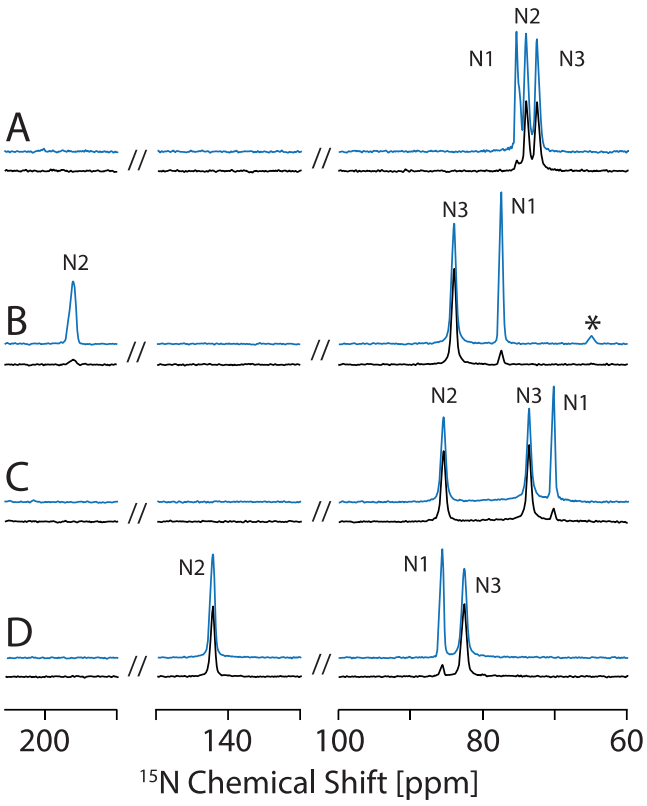

Figure 2. ^{1}H→^{15}N CP/MAS spectra acquired using (black) 200 μs and (blue) 5 ms contact times for (A) **Crea·H$_2$O**, (B) **CreaT**, (C) **CreaHCl**, and (D) **CreaTHCl** at 14.1 T, 100 K, and ν_{rot} = 8 kHz. The asterisk denotes a spinning sideband.

protonated moieties, N2 and N3 sites in **Crea·H$_2$O**, **CreaHCl**, and **CreaTHCl**, and N3 in **CreaT**.

3.2.3. ^{35}Cl{^{1}H} SSNMR. The ^{35}Cl{^{1}H} SSNMR spectra of **CreaHCl** and **CreaTHCl** were acquired under static and MAS conditions at 18.8 T and under static conditions at 14.1 T (Figure 3). Each spectrum features a single central transition (CT, +1/2 ↔ −1/2) powder pattern influenced by the second-order quadrupolar interaction and chemical shift anisotropy. From the static experiments, spectra from the Fourier transform of both the coadded CPMG train (93 echoes for **CreaHCl** at both 14.1 and 18.8 T, and 93 and 47 echoes for **CreaTHCl** at 14.1 and 18.8 T, respectively) and the first echo in the CPMG train are displayed, since there are clear intensity differences that may arise from anisotropy in the

Table 3. Experimental and Calculated ^{15}N Isotropic Chemical Shifts[a]

		N1 (ppm)	N2 (ppm)	N3 (ppm)	Δ^{CS}_{RMSD} (ppm)[b]
Crea·H$_2$O	exp.	75.3(6)	74.1(6)	72.4(6)	
	calc.	80.0	69.9	69.4	4.04
CreaT	exp.	77.2(5)	196.0(10)	83.9(7)	
	calc.	82.5	204.3	78.9	6.35
CreaHCl	exp.	70.2(5)	85.5(7)	73.6(6)	
	calc.	75.1	79.1	70.2	5.04
CreaTHCl	exp.	85.6(6)	142.2(6)	82.6(7)	
	calc.	90.7	146.9	80.4	4.22

[a]Atomic numbering scheme is provided in Scheme 1. [b]The agreement between calculated (δ_i^{calc}) and experimental (δ_i^{exp}) isotropic chemical shifts was compared using a chemical shift root-mean-square deviation (Δ^{CS}_{RMSD}): $\Delta^{CS}_{RMSD} = \sqrt{\frac{\sum_{i=1}^{N}(\delta_i^{calc} - \delta_i^{exp})^2}{N}}$ where N is the total number of isotropic chemical shifts.

effective T_2, T_2^{eff} (Figure S5). These spectra reveal that both **CreaHCl** and **CreaTHCl** have one Cl$^-$ ion in the asymmetric unit, again consistent with the Z' = 1 observations above. Spectral simulations of the MAS spectra and static spectra corresponding to the first echo were used to extract the EFG and chemical shift tensor parameters, as well as the Euler angles describing their relative orientations (Table 4).

3.3. QNMRX-CSP of CreaHCl

Before discussing the relationships between NMR interaction tensors and the unique molecular structures of each solid form of creatine and creatinine, it is necessary to determine the crystal structure of **CreaHCl**, which is heretofore unknown. Detailed below is a description of our application of QNMRX-CSP to this problem, which is also summarized in Scheme S1 and Table 5.

A creatine cation with the positive charge distributed about the guanidium functional group was built in a $P1$ 15 × 15 × 15 Å^3 box and subjected to a DFT-D2* convergent geometry optimization. A Cl$^-$ ion was added to the asymmetric unit, and Hirshfeld charges were assigned (Table S7). The creatine cation and Cl$^-$ ion were assigned as independent motion groups. A MC-SA approach within Polymorph (section 2.4.2) was used to obtain 50,620 candidate structures. Candidate structures were retained using Metric Set 1 (Table S5), resulting in 464 structures. Subsequently, these underwent truncated DFT-D2* geometry optimizations and were retained

https://doi.org/10.1021/acs.molpharmaceut.6c00077
Mol. Pharmaceutics 2026, 23, 3397−3409

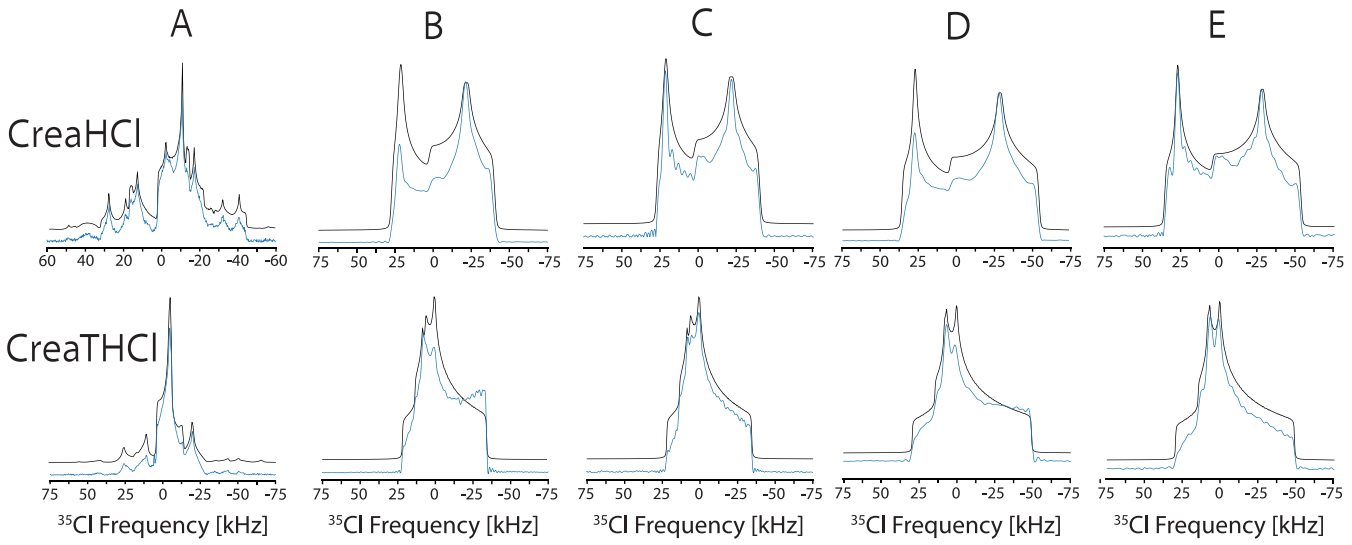

Figure 3. Experimental (blue) and simulated (black) ^{35}Cl{^{1}H} SSNMR for **CreaHCl** and **CreaTHCl** acquired at 18.8 T under (A) MAS and (B, C) static conditions and at (D, E) 14.1 T under static conditions. The static spectra are either the coadded spectra (B, D) or the Fourier transform of the first echo (C, E). The Fourier transforms of the individual echoes in the CPMG train static spectra acquired at 18.8 T are provided in Figure S4.

Table 4. Experimental and Calculated ^{35}Cl EFG and Chemical Shift Tensor Parameters[a,b,c,d]

		C_Q (MHz)	η_Q	δ_{iso} (ppm)	Ω (ppm)	κ	α (°)	β (°)	γ (°)
CreaHCl	exp.	5.70(2)	0.29(2)	53(3)	76(10)	−0.10(20)	355(10)	27(10)	247(10)
	calc.	−5.398	0.26	51.5	88.5	−0.03	301	10	337
CreaTHCl	exp.	4.42(5)	0.92(3)	57(2)	84(5)	−0.75(10)	190(10)	40(5)	90(5)
	calc.	4.159	0.85	64.6	93.2	−0.66	230	87	176

[a]The principal components of the EFG tensors are defined such that $|V_{33}| \geq |V_{22}| \geq |V_{11}|$. The quadrupolar coupling constant and asymmetry parameter are given by $C_Q = eQV_{33}/h$, and $\eta_Q = (V_{11} - V_{22})/V_{33}$, respectively. The sign of C_Q cannot be determined from the experimental ^{35}Cl spectra. [b]The principal components of the chemical shift tensors are defined using the frequency-ordered convention, with $\delta_{11} \geq \delta_{22} \geq \delta_{33}$. The isotropic chemical shift, span, and skew are given by $\delta_{iso} = (\delta_{11} + \delta_{22} + \delta_{33})/3$, $\Omega = \delta_{11} - \delta_{33}$, and $\kappa = 3(\delta_{22} - \delta_{iso})/\Omega$, respectively. [c]The Euler angles α, β, and γ define the relative orientation of the EFG and chemical shift tensors using the $ZY'Z''$ convention for rotation. [d]^{35}Cl chemical shielding values were converted to the chemical shift scale by calculating the ^{35}Cl chemical shielding on a DFT-D2* geometry-optimized structural model of *L*-histidine HCl·H_2O (HISTCM01) and setting its chemical shift to 34.5 ppm.[66]

Table 5. Summary of the Number of Candidate Structures Derived Using QNMRX-CSP

Metric Set #	initial		retained
1	50,620	→	464
2	464	→	138
3	138	→	25
4	25	→	5

using Metric Set 2, leading to 138 candidate structures. The 138 candidate structures then underwent convergent DFT-D2* geometry optimizations and were retained using Metric Set 3, leading to 25 candidate structures. These candidate structures had their unit cell parameters adjusted to match those obtained by indexing the PXRD pattern of **CreaHCl** (Table 1) and subjected to a final round of convergent geometry optimizations, followed by retention of 5 candidate structures via application of Metric Set 4. All five structural models exhibit similar packing motifs, indicative of the same local energy minima and small differences in ΔE_{lat}. Their calculated ^{35}Cl EFG tensors agree well with experimental values, as they all fall below the benchmark threshold of $\Gamma_{EFG} \leq 0.49$ MHz (Table 6), indicating that the structural models are consistent with the ^{35}Cl SSNMR data. These structural models also yield simulated PXRD patterns that visually align

Table 6. Structural Validation for the Candidate Structures from QNMRX-CSP

structure #	Γ_{EFG} (MHz)	ΔE_{lat} (kJ/mol)[a]	Δ^{AP}_{RMSD} (Å)[b]	R (%)[c]
SCXRD	2.20	387.814	0.000/0.047	25.20/0.00/1.43
SCXRD*	0.19	−0.025	0.047/0.000	24.12/1.45/0.00
9−695	0.22	0	0.052/0.008	24.40/1.07/0.37
4−78	0.22	0	0.057/0.013	24.09/1.48/0.03
9−705	0.19	0.003	0.057/0.013	24.23/1.29/0.15
9−160	0.22	0.010	0.058/0.014	23.99/1.62/0.17
10−602	0.21	0.012	0.057/0.014	24.04/1.55/0.10

[a]The static lattice energy difference (ΔE_{lat}) between the five structural models from QNMRX-CSP, normalized such that the lowest energy structure is E_{lat} = 0 kJ mol^{-1}. For SCXRD* and SCXRD, the ΔE_{lat} values are reported with respect to 9−695 and 4−78 having E_{lat} = 0 kJ mol^{-1}. [b]Δ^{AP}_{RMSD} values are calculated by comparing the QNMRX-CSP structural model to the SCXRD structure (left), and to the convergent geometry-optimized SCXRD structure (right). [c]*R*-factors calculated using the simulated PXRD patterns for the structural models from QNMRX-CSP are compared to the experimental PXRD pattern (left), the simulated PXRD pattern of the SCXRD structure (middle), and the simulated PXRD pattern of the geometry-optimized SCXRD structure (right).

https://doi.org/10.1021/acs.molpharmaceut.6c00077
Mol. Pharmaceutics 2026, 23, 3397−3409

well with the experimental pattern (Figure 4), providing qualitative agreement between the experimental and the simulated patterns (*vide infra*).

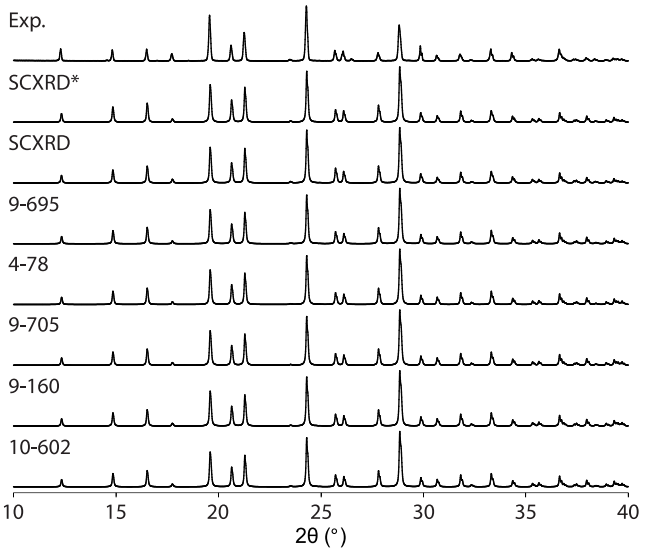

Figure 4. Experimental PXRD pattern of **CreaHCl** (top) and the simulated PXRD patterns from the SCXRD structure (SCXRD), DFT-D2* geometry-optimized SCXRD structure (SCXRD*), and five candidate structures from QNMRX-CSP.

3.4. Single-Crystal X-ray Diffraction

SCXRD data were acquired on a single crystal of **CreaHCl** and used to determine its crystal structure (Table S1). Visual comparisons of the QNMRX-CSP and the SCXRD structures of **CreaHCl** reveal similar packing motifs (Figure 5) and good quantitative agreement with R and Δ^{AP}_{RMSD}, *ca.* 1.4% and 0.056 Å, respectively (Table 6). Further improvements in both R and Δ^{AP}_{RMSD} are observed from comparisons of the simulated PXRD patterns from the QNMRX-CSP structures with those simulated from the DFT-D2* geometry-optimized SCXRD structure (denoted SCXRD* in Figure 4 and Table 6), to *ca.* 0.10% and 0.012 Å. These improvements are largely attributed to the refinement of the hydrogen atom positions and indicate that the QNMRX-CSP and SCXRD structures are in the same local energy minima.

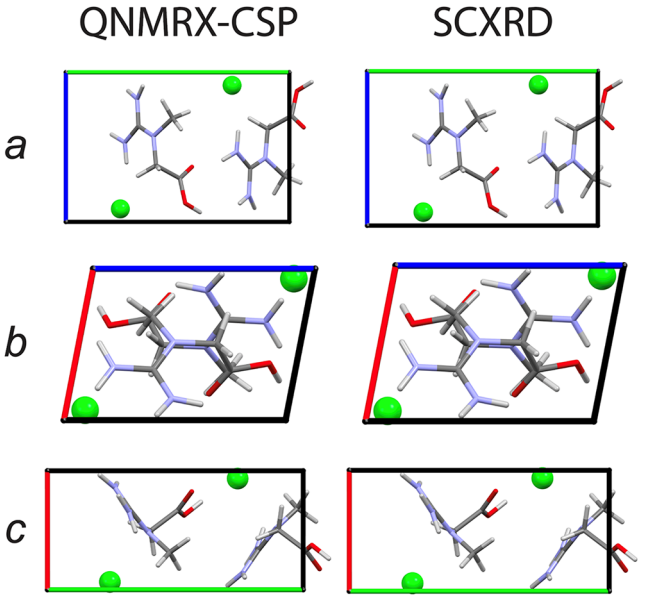

Figure 5. Crystal structures of **CreaHCl** from QNMRX-CSP (structure 9−695) and SCXRD data viewed along the three crystallographic axes.

The validation of the QNMRX-CSP structures via comparisons to the SCXRD and SCXRD* structures allows for further analysis of the experimental PXRD pattern of **CreaHCl**, where a peak at *ca.* 26.5° corresponds to some impurity phase, since it does not appear in the PXRD patterns of the other samples (Figure S3). This also supports the conclusion that the impurity peak observed in the ^{13}C SSNMR spectra of **CreaHCl** does not correspond to that of **CreaTHCl**.

3.5. NMR Tensor Calculations and Peak Assignments

Chemical shifts obtained from DFT calculations can fully or partially assist in peak assignments; however, their reliability depends on the accuracy of the computational method as well as the nature of the structural model. Benchmarked GIPAW calculated chemical shifts on DFT-D2* refined structural models yield chemical shift RMSD (Δ^{CS}_{RMSD}, Tables 2, 3) values of 3.1 ppm for ^{13}C and 5.2 ppm for ^{15}N,[74,75] supporting their utility for peak assignments when the experimental chemical shift differences significantly exceed these values.

3.5.1. ^{13}C Chemical Shifts. The calculated ^{13}C chemical shifts are in good agreement with experiment, with Δ^{CS}_{RMSD} values ranging from 2.64 to 3.72 ppm, allowing for the unambiguous assignment of the peaks to carbon atoms (Table 2; Figure 1).

3.5.2. ^{15}N Chemical Shifts. Most of the chemical shifts in the ^{15}N spectra occur in narrow bands $\lesssim$ 15 ppm, which makes peak assignment from ^{15}N chemical shift calculations alone challenging, since the calculated ^{15}N chemical shifts have Δ^{CS}_{RMSD} values ranging from 4.04 to 6.35 ppm (Table 3). Hence, better assignments were made using ^{1}H−^{15}N variable-contact time CP/MAS NMR experiments (*cf.* section 3.2).

The experimental ^{15}N chemical shift difference for the two RNH_2 groups (sites N2 and N3) in **CreaHCl** is *ca.* 12 ppm. Here, chemical shift calculations aid in peak assignment, showing that the RNH_2 moiety at site N2 (δ_{iso} = 85.5 ppm) makes two H···Cl contacts, whereas that at N3 (δ_{iso} = 73.6 ppm) has H···Cl and H···O contacts, accounting for their distinct chemical shifts (Figure 6). The chemical shift assignments for the RNH_2 moieties (sites N2 and N3) in **Crea·H$_2$O** cannot be made solely with DFT calculations due to their small chemical shift difference ($\lesssim$ 1.5 ppm), which lies below the lower bound of Δ^{CS}_{RMSD} values. Tentative assignments were made by assigning the experimental ^{15}N chemical shifts to the calculated values that yielded the smallest Δ^{CS}_{RMSD} value. Further improvements in these assignments could come from more accurate calculations of ^{15}N chemical shifts or the use of advanced experimental techniques. For instance, two-dimensional ^{1}H−^{15}N ID-HETCOR experiments[76] may resolve this issue as the two NH_2 sites differ in their hydrogen bonding environments. One forms H···O hydrogen bonds of r(H···O) = 1.92 and 1.10 Å with the deprotonated carboxylic acid, while the other interacts with both a carboxylic acid and a water molecule, with r(H···O) = 1.85 and 2.09 Å, respectively. However, such experiments would require fast MAS rates, ν_{rot} $\gtrsim$ 50 kHz, which are unfeasible with our equipment at 100 K. While achievable at room temperature, these conditions likely necessitate ^{15}N isotopic enrichment to obtain a sufficient

https://doi.org/10.1021/acs.molpharmaceut.6c00077
Mol. Pharmaceutics 2026, 23, 3397−3409

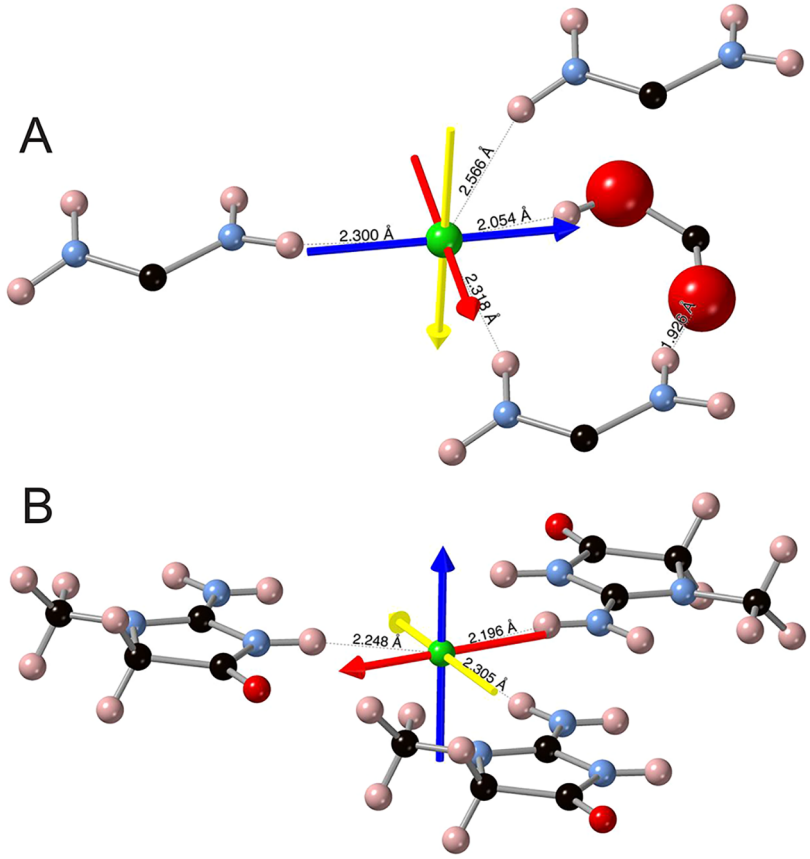

Figure 6. ^{35}Cl EFG tensor components V_{11} (red), V_{22} (yellow), and V_{33} (blue) and the surrounding environment of the Cl^- ions in (A) **tHCl** and (B) **CreaTHCl**.

signal-to-noise ratio in a reasonable time. Alternatively, the measurement of the ^{15}N chemical shift tensors may help differentiate these two sites.

CreaT and **CreaTHCl** each feature RNH_2 and $R_1R_2NCH_3$ moieties, as well as an imidazole (R_1R_2N) moiety where the N is deprotonated or protonated, respectively. These peak assignments are trivial, even without DFT calculations. For **CreaT**, only the RNH_2 resonance is intense at both contact times, whereas for **CreaTHCl**, both the RNH_2 and protonated imidazole resonances show this behavior. In addition, the calculated ^{15}N chemical shifts agree with the large chemical shift differences observed in the experimental spectra.

3.5.3. ^{35}Cl Electric Field Gradient Tensors. The values of $C_Q(^{35}Cl)$ and η_Q for Cl^- ions in organic HCl salts are well-known to be influenced by H···Cl^- hydrogen bonds (i.e., r(H···Cl) < 2.6 Å);[77] in particular, the number of short contacts (i.e., $r(H\cdots Cl^-) \lesssim 2.2$ Å) and their arrangement have the strongest influences on the ^{35}Cl EFG tensor.[23,26,27] For instance, the large value of C_Q and low value of η_Q for **CreaHCl** suggest that the structure features a single short contact (i.e., $r(H\cdots Cl^-) \lesssim 2.2$ Å), and the EFG tensor is oriented such that the largest component (V_{33}) points along or near the direction of this short contact. The **CreaHCl** structure determined from QNMRX-CSP reveals that the Cl^- ion environment has four H···Cl^- hydrogen bonds (Figure 6A), though only the COOH···Cl^- hydrogen bond is representative of a short contact ($r(H\cdots Cl^-) = 2.05$ Å); as such, V_{33} is oriented near this bond.

The large C_Q and high η_Q for **CreaTHCl** suggest a very different arrangement of H···Cl^- hydrogen bonds.[23,26,27] The DFT-D2* geometry-optimized structural model of **CreaTHCl** reveals that the Cl^- ion environment has three H···Cl^- hydrogen bonds (Figure 6B), with only one of the RNH_2 moieties making a short contact, though on the "long side" of short contact ($r(H\cdots Cl^-) \lesssim 2.196$ Å). Interestingly, the three hydrogen atoms from these three H···Cl bonds form an almost planar triangle around the Cl^- ion, $\sum[\angle(H\cdots Cl^-\cdots H)] = 359.98°$, with V_{33} oriented approximately perpendicular to this plane, and V_{11} oriented near the shortest contact.

The opposite signs of the C_Q values for **CreaHCl** and **CreaTHCl** (i.e., −5.398 and 4.159 MHz, respectively) are consistent with many previous calculations of ^{35}Cl EFG tensors where V_{33} is directed near ($V_{33} > 0$) or perpendicular to ($V_{33} < 0$) a single short H···Cl^- contact, respectively.[23,26,27] We note that these signs are available only from calculations and cannot be determined directly from the ^{35}Cl SSNMR spectra.

4. CONCLUSIONS

We have demonstrated that PXRD and multinuclear SSNMR are effective methods for distinguishing the different solid forms of creatine and creatinine, detecting impurity phases, and enabling *de novo* structural determination. However, given the complementary strengths and limitations of each method, their combined application is strongly advised. PXRD is a rapid and accessible method for characterizing the different solid forms; however, despite being able to observe an impurity phase in **CreaHCl**, challenges still remain when trying to resolve small-weight-percent impurities that may go undetected. ^{13}C SSNMR was found to be a rapid and effective method for characterizing **Crea·H_2O** and **CreaT**, as both

https://doi.org/10.1021/acs.molpharmaceut.6c00077
Mol. Pharmaceutics 2026, 23, 3397−3409

featured distinct chemical shifts with minimal spectral overlap. In contrast, the ^{13}C SSNMR of **CreaHCl** and **CreaTHCl** is less informative due to their similar chemical shifts, making it difficult to distinguish between the two solid forms. Nonetheless, one additional peak is present in the spectra of the former, indicating the presence of an unknown impurity phase. ^{15}N SSNMR is an effective method for characterizing all of the materials studied herein. However, acquiring ^{15}N spectra is challenging due to the low natural abundance, which requires long signal averaging times. To circumvent this, ^{15}N spectra were acquired at 100 K. This approach, however, has limitations, including the need for cryogenic equipment that can handle such low temperatures and the risk of phase transitions in some materials under these low-temperature conditions. Nonetheless, ^{15}N SSNMR could be effective for detecting impurity phases from the desired product. The ^{35}Cl SSNMR spectra of **CreaHCl** and **CreaTHCl** are distinct and enable their spectral fingerprinting. However, small-weight-percent impurities may be missed due to spectral overlap and powder pattern distortions arising from T_2 anisotropy. Additionally, the ^{35}Cl spectra provide insights into the complex hydrogen bonding networks involving the Cl^- ion and yield ^{35}Cl EFG tensor parameters, which were critical for QNMRX-CSP. QNMRX-CSP was subsequently used for the *de novo* structural determination of **CreaHCl**, which, despite being commercially available, had no previously reported crystal structure. Subsequent SCXRD experiments were used to determine the structure of **CreaHCl**, validating the structural model determined from QNMRX-CSP. These results demonstrate the potential of QNMRX-CSP for the *de novo* structure determination in the absence of SCXRD data and its broader application to other pharmaceutically and nutraceutically relevant organic HCl salts. It is hoped that the results herein will encourage future use of PXRD and SSNMR for the characterization of the many solid forms of creatine and related byproducts, and perhaps even the QNMRX-CSP determination of more crystal structures of these important compounds.

■ ASSOCIATED CONTENT

Supporting Information

The Supporting Information is available free of charge at https://pubs.acs.org/doi/10.1021/acs.molpharmaceut.6c00077.

A schematic overview of QNMRX-CSP, the linear regressions for converting chemical shieldings to the chemical shift scale, simulated and experimental XRD patterns, additional SSNMR spectra and experimental details, and a description of the Hirshfeld charges for QNMRX-CSP (PDF)

Creatine supplementary structures (ZIP)

■ AUTHOR INFORMATION

Corresponding Author

Sean T. Holmes − *Department of Chemistry & Biochemistry, Florida State University, Tallahassee, Florida 32306, United States; National High Magnetic Field Laboratory, Tallahassee, Florida 32310, United States;* orcid.org/0000-0002-5821-9641; Email: sholmes2@fsu.edu

Authors

Carl H. Fleischer, III − *Department of Chemistry & Biochemistry, Florida State University, Tallahassee, Florida 32306, United States; National High Magnetic Field Laboratory, Tallahassee, Florida 32310, United States;* orcid.org/0000-0002-1333-4195

Victoria K. Rash − *Department of Physics, University of Texas at Dallas, Richardson, Texas 75080, United States*

Zach T. Dowdell − *Department of Chemistry & Biochemistry, Florida State University, Tallahassee, Florida 32306, United States; National High Magnetic Field Laboratory, Tallahassee, Florida 32310, United States*

Sara Termos − *Department of Chemistry & Biochemistry, Florida State University, Tallahassee, Florida 32306, United States; National High Magnetic Field Laboratory, Tallahassee, Florida 32310, United States*

Xinsong Lin − *Department of Chemistry & Biochemistry, Florida State University, Tallahassee, Florida 32306, United States*

Shubha S. Gunaga − *National High Magnetic Field Laboratory, Tallahassee, Florida 32310, United States*

Frédéric Mentink-Vigier − *National High Magnetic Field Laboratory, Tallahassee, Florida 32310, United States;* orcid.org/0000-0002-3570-9787

Juan Jimenez − *Chemistry Division, Brookhaven National Laboratory, Upton, New York 11973, United States;* orcid.org/0000-0003-4710-1047

A. M. Milinda Abeykoon − *National Synchrotron Light Source II, Brookhaven National Laboratory, Upton, New York 11973, United States*

Sanjaya Senanayake − *Chemistry Division, Brookhaven National Laboratory, Upton, New York 11973, United States;* orcid.org/0000-0003-3991-4232

[#]**Robert W. Schurko** − *Department of Chemistry & Biochemistry, Florida State University, Tallahassee, Florida 32306, United States; National High Magnetic Field Laboratory, Tallahassee, Florida 32310, United States;* orcid.org/0000-0002-5093-400X

Complete contact information is available at: https://pubs.acs.org/10.1021/acs.molpharmaceut.6c00077

Notes

The authors declare no competing financial interest.

[#]Deceased on February 20, 2026.

■ ACKNOWLEDGMENTS

R.W.S. and C.H.F. are grateful for research support from The Florida State University and the National High Magnetic Field Laboratory (NHMFL), which is funded by the National Science Foundation Cooperative Agreement (DMR-2128556) and by the State of Florida. V.K.R. was supported by the National Science Foundation Research Experiences for Undergraduates program. We are grateful to the National Institutes of Health for support through the National Resource for Advanced NMR Technology (RM1 GM148766), which provides resources for optimizing our 600 MHz DNP platform and supports postdoctoral funding for S.G. This work was supported in part by the U.S. Department of Energy, Office of Science, Office of Basic Energy Sciences, under Award Number DE-SC0022310, covering expenses related to postdoctoral salary of S.T.H., which aided in the development of quantum

chemical computational methods used herein and in other projects.

REFERENCES

(1) Hespel, P.; Derave, W. Ergogenic Effects of Creatine in Sports and Rehabilitation. In *Creatine and Creatine Kinase in Health and Disease*; Springer Netherlands: Dordrecht, 2007; Vol. *46*, pp 246−259 DOI: 10.1007/978-1-4020-6486-9_12.

(2) Tarnopolsky, M. A. Clinical Use of Creatine in Neuromuscular and Neurometabolic Disorders. In *Creatine and Creatine Kinase in Health and Disease*; Springer Netherlands: Dordrecht, 2007; Vol. *46*, pp 183−204 DOI: 10.1007/978-1-4020-6486-9_10.

(3) Klein, A. M.; Ferrante, R. J. The Neuroprotective Role of Creatine. In *Creatine and Creatine Kinase in Health and Disease*; Springer Netherlands: Dordrecht, 2007; Vol. *46*, pp 205−243 DOI: 10.1007/978-1-4020-6486-9_11.

(4) Kreider, R. B.; Jäger, R.; Purpura, M. Bioavailability, Efficacy, Safety, and Regulatory Status of Creatine and Related Compounds: A Critical Review. *Nutrients* **2022**, *14* (5), 1035.

(5) Pischel, I.; Gastner, T. Creatine − Its Chemical Synthesis, Chemistry, and Legal Status. In *Creatine and Creatine Kinase in Health and Disease*; Springer Netherlands: Dordrecht, 2007; Vol. *46*, pp 291−307 DOI: 10.1007/978-1-4020-6486-9_15.

(6) Gangopadhyay, D.; Sharma, P.; Singh, S. K.; Singh, P.; Tarcea, N.; Deckert, V.; Popp, J.; Singh, R. K. Raman Spectroscopic Approach to Monitor the in Vitro Cyclization of Creatine → Creatinine. *Chem. Phys. Lett.* **2015**, *618*, 225−230.

(7) Gangopadhyay, D.; Sharma, P.; Singh, S. K.; Singh, P.; Deckert, V.; Popp, J.; Singh, R. K. Surface Enhanced Raman Scattering Based Reaction Monitoring of: In Vitro Decyclization of Creatinine → Creatine. *RSC Adv.* **2016**, *6* (64), 58943−58949.

(8) Qiu, S.; Cai, X.; Yuan, Y.; Xie, B.; Sun, Z.; Wu, T. Changes in Creatinine-to-Cystatin C Ratio over 4 Years, Risk of Diabetes, and Cardiometabolic Control: The China Health and Retirement Longitudinal Study. *J. Diabetes* **2021**, *13* (12), 1025−1033.

(9) Zhou, S.; Wang, P.; Sun, L.; Zhao, X.; Gong, C.; Yang, Y.; Ren, W.; Yang, Y.; Zhang, Q.; Jiang, J. J. Lower Serum Creatinine to Cystatin C Ratio Associated with Increased Incidence of Frailty in Community-Dwelling Elderly Men but Not in Elderly Women. *Aging Clin. Exp. Res.* **2024**, *36* (1), No. 140, DOI: 10.1007/s40520-024-02787-7.

(10) Kang, H. G.; Lee, H. K.; Cho, K. B.; Park, S. Il. A Review of Natural Products for Prevention of Acute Kidney Injury. *Medicina* **2021**, *57* (11), No. 1266.

(11) Jayasekhar Babu, P.; Tirkey, A.; Mohan Rao, T. J.; Chanu, N. B.; Lalchhandama, K.; Singh, Y. D. Conventional and Nanotechnology Based Sensors for Creatinine (A Kidney Biomarker) Detection: A Consolidated Review. *Anal. Biochem.* **2022**, *645*, No. 114622.

(12) Kashani, K.; Rosner, M. H.; Ostermann, M. Creatinine: From Physiology to Clinical Application. *Eur. J. Intern. Med.* **2020**, *72*, 9−14, DOI: 10.1016/j.ejim.2019.10.025.

(13) Harris, R. K. NMR Crystallography: The Use of Chemical Shifts. *Solid State Sci.* **2004**, *6* (10), 1025−1037.

(14) Martineau, C.; Senker, J.; Taulelle, F. NMR Crystallography. In *Annual Reports on NMR Spectroscopy*; Webb, G. A., Ed.; John Wiley & Sons Ltd.: New York, NY, 2014; Vol. *82*, pp 1−57 DOI: 10.1016/B978-0-12-800184-4.00001-1.

(15) Martineau, C. NMR Crystallography: Applications to Inorganic Materials. *Solid State Nucl. Magn. Reson.* **2014**, *63*−*64*, 1−12.

(16) Hodgkinson, P. NMR Crystallography of Molecular Organics. *Prog. Nucl. Magn. Reson. Spectrosc.* **2020**, *118*−*119*, 10−53.

(17) *Modern NMR Crystallography*; Bryce, D. L., Ed.; Royal Society of Chemistry, 2025. DOI: 10.1039/9781837673179.

(18) Peach, A. A.; Fleischer, C. H.; Levin, K.; Holmes, S. T.; Sanchez, J. E.; Schurko, R. W. Quadrupolar NMR Crystallography Guided Crystal Structure Prediction (QNMRX-CSP). *CrystEngComm* **2024**, *26* (35), 4782−4803.

(19) Fleischer, C. H.; Holmes, S. T.; Levin, K.; Veinberg, S. L.; Schurko, R. W. Characterization of Ephedrine HCl and Pseudoephedrine HCl Using Quadrupolar NMR Crystallography Guided Crystal Structure Prediction. *Faraday Discuss.* **2025**, *255*, 88−118.

(20) Fleischer, C. H.; Holmes, S. T.; Lin, X.; Schurko, R. W. De Novo Crystal Structure Determination of L-Alaninamide HCl by Quadrupolar NMR Crystallography Guided Crystal Structure Prediction (QNMRX-CSP). *Solid State Nucl. Magn. Reson.* **2025**, *140*, No. 102034.

(21) Fleischer, C. H.; Holmes, S. T.; Schurko, R. W. Quadrupolar NMR Crystallography Guided Crystal Structure Prediction (QNMRX-CSP) of Zwitterionic Organic HCl Salts. *CrystEngComm* **2025**, *27*, 7379.

(22) Bryce, D. L.; Sward, G. D. Chlorine-35/37 NMR Spectroscopy of Solid Amino Acid Hydrochlorides: Refinement of Hydrogen-Bonded Proton Positions Using Experiment and Theory. *J. Phys. Chem. B* **2006**, *110* (51), 26461−26470.

(23) Hamaed, H.; Pawlowski, J. M.; Cooper, B. F. T.; Fu, R.; Eichhorn, S. H.; Schurko, R. W. Application of Solid-State 35Cl NMR to the Structural Characterization of Hydrochloride Pharmaceuticals and Their Polymorphs. *J. Am. Chem. Soc.* **2008**, *130* (33), 11056−11065.

(24) Hildebrand, M.; Hamaed, H.; Namespetra, A. M.; Donohue, J. M.; Fu, R.; Hung, I.; Gan, Z.; Schurko, R. W. 35Cl Solid-State NMR of HCl Salts of Active Pharmaceutical Ingredients: Structural Prediction, Spectral Fingerprinting and Polymorph Recognition. *CrystEngComm* **2014**, *16* (31), 7334−7356.

(25) Peach, A. A.; Hirsh, D. A.; Holmes, S. T.; Schurko, R. W. Mechanochemical Syntheses and 35Cl Solid-State NMR Characterization of Fluoxetine HCl Cocrystals. *CrystEngComm* **2018**, *20* (20), 2780−2792.

(26) Holmes, S. T.; Vojvodin, C. S.; Veinberg, N.; Iacobelli, E. M.; Hirsh, D. A.; Schurko, R. W. Hydrates of Active Pharmaceutical Ingredients: A 35Cl and 2H Solid-State NMR and DFT Study. *Solid State Nucl. Magn. Reson.* **2022**, *122*, No. 101837.

(27) Holmes, S. T.; Hook, J. M.; Schurko, R. W. Nutraceuticals in Bulk and Dosage Forms: Analysis by 35Cl and 14N Solid-State NMR and DFT Calculations. *Mol. Pharmaceutics* **2022**, *19* (2), 440−455.

(28) Akkermans, R. L. C.; Spenley, N. A.; Robertson, S. H. Monte Carlo Methods in Materials Studio. *Mol. Simul.* **2013**, *39* (14−15), 1153−1164.

(29) Holmes, S. T.; Vojvodin, C. S.; Schurko, R. W. Dispersion-Corrected DFT Methods for Applications in Nuclear Magnetic Resonance Crystallography. *J. Phys. Chem. A* **2020**, *124* (49), 10312−10323.

(30) Arakali, A. V.; McCloskey, J.; Parthasarathy, R.; Alderfer, J. L.; Chheda, G. B.; Srikrishnan, T. Study of Creatinine and Its 5-Alkoxy Analogs: Structure and Conformational Studies in the Solid and Solution States by x-Ray Crystallography, NMR, UV and Mass Spectrometry. *Nucleosides Nucleotides* **1997**, *16* (12), 2193−2218.

(31) Tabatabaee, M.; Sharif, M. A.; Dušek, M.; Pojarová, M. 2-Amino-1methyl-4-Oxo-4,5-Dihydro-1H-Imidazol-3-Ium Chloride. *Acta Crystallogr., Sect. E* **2012**, *68* (7), 02183−02184, DOI: 10.1107/S1600536812027080.

(32) Bell, T. W.; Hou, Z.; Luo, Y.; Drew, M. G. B.; Chapoteau, E.; Czech, B. P.; Kumar, A. Detection of Creatinine by a Designed Receptor. *Science* **1995**, *269* (5224), 671−674.

(33) Neumann, M. A. X-Cell: A Novel Indexing Algorithm for Routine Tasks and Difficult Cases. *J. Appl. Crystallogr.* **2003**, *36* (2), 356−365.

(34) Sheldrick, G. M. SHELXT − Integrated Space-Group and Crystal-Structure Determination. *Acta Crystallogr., Sect. A* **2015**, *71* (1), 3−8.

(35) Sheldrick, G. M. Crystal Structure Refinement with SHELXL. *Acta Crystallogr., Sect. C* **2015**, *71* (1), 3−8.

(36) Hall, D. A.; Maus, D. C.; Gerfen, G. J.; Inati, S. J.; Becerra, L. R.; Dahlquist, F. W.; Griffin, R. G. Polarization-Enhanced NMR Spectroscopy of Biomolecules in Frozen Solution. *Science* **1997**, *276* (5314), 930−932.

https://doi.org/10.1021/acs.molpharmaceut.6c00077
Mol. Pharmaceutics 2026, 23, 3397−3409

(37) Lesage, A.; Lelli, M.; Gajan, D.; Caporini, M. A.; Vitzthum, V.; Miéville, P.; Alauzun, J.; Roussey, A.; Thieuleux, C.; Mehdi, A.; Bodenhausen, G.; Copéret, C.; Emsley, L. Surface Enhanced NMR Spectroscopy by Dynamic Nuclear Polarization. *J. Am. Chem. Soc.* **2010**, *132* (44), 15459−15461.
(38) Pines, A.; Gibby, M. G.; Waugh, J. S. Proton-Enhanced Nuclear Induction Spectroscopy 13C Chemical Shielding Anisotropy in Some Organic Solids. *Chem. Phys. Lett.* **1972**, *15* (3), 373−376.
(39) Pines, A.; Gibby, M. G.; Waugh, J. S. Proton-Enhanced NMR of Dilute Spins in Solids. *J. Chem. Phys.* **1973**, *59* (2), 569−590.
(40) Peersen, O. B.; Wu, X. L.; Kustanovich, I.; Smith, S. O. Variable-Amplitude Cross-Polarization MAS NMR. *J. Magn. Reson., Ser. A* **1993**, *104* (3), 334−339.
(41) Metz, G.; Wu, X. L.; Smith, S. O. Ramped-Amplitude Cross Polarization in Magic Angle Spinning NMR. *J. Magn. Reson., Ser. A* **1994**, *110* (2), 219−227.
(42) Schaefer, J.; Stejskal, E. O. Carbon-13 Nuclear Magnetic Resonance of Polymers Spinning at the Magic Angle. *J. Am. Chem. Soc.* **1976**, *98* (4), 1031−1032.
(43) Mentink-Vigier, F.; Marin-Montesinos, I.; Jagtap, A. P.; Halbritter, T.; Van Tol, J.; Hediger, S.; Lee, D.; Sigurdsson, S. T.; De Paëpe, G. Computationally Assisted Design of Polarizing Agents for Dynamic Nuclear Polarization Enhanced NMR: The AsymPol Family. *J. Am. Chem. Soc.* **2018**, *140* (35), 11013−11019.
(44) Taylor, R. E. 13C CP/MAS: Application to Glycine. *Concepts Magn. Reson., Part A* **2004**, *22A* (2), 79−89.
(45) Bertani, P.; Raya, J.; Bechinger, B. 15N Chemical Shift Referencing in Solid State NMR. *Solid State Nucl. Magn. Reson.* **2014**, *61*−*62*, 15−18.
(46) Larsen, F. H.; Jakobsen, H. J.; Ellis, P. D.; Nielsen, N. C. Sensitivity-Enhanced Quadrupolar-Echo NMR of Half-Integer Quadrupolar Nuclei. Magnitudes and Relative Orientation of Chemical Shielding and Quadrupolar Coupling Tensors. *J. Phys. Chem. A* **1997**, *101* (46), 8597−8606.
(47) Hahn, E. L. Spin Echoes. *Phys. Rev.* **1950**, *80* (4), 580−594.
(48) Chan, J. C. C. Spin Echoes in Half-Integer Quadrupole Systems. *Concepts Magn. Reson.* **1999**, *11* (6), 363−377.
(49) Chapman, R. P.; Widdifield, C. M.; Bryce, D. L. Solid-State NMR of Quadrupolar Halogen Nuclei. *Prog. Nucl. Magn. Reson. Spectrosc.* **2009**, *55* (3), 215−237.
(50) van Meerten, S. G. J.; Franssen, W. M. J.; Kentgens, A. P. M. SsNake: A Cross-Platform Open-Source NMR Data Processing and Fitting Application. *J. Magn. Reson.* **2019**, *301*, 56−66.
(51) Clark, S. J.; Segall, M. D.; Pickard, C. J.; Hasnip, P. J.; Probert, M. I. J.; Refson, K.; Payne, M. C. First Principles Methods Using CASTEP. *Z. Kristallogr.* **2005**, *220* (5−6), 567−570.
(52) Hammer, B.; Hansen, L. B.; Nørskov, J. K. Improved Adsorption Energetics within Density-Functional Theory Using Revised Perdew-Burke-Ernzerhof Functionals. *Phys. Rev. B* **1999**, *59* (11), 7413−7421.
(53) van Lenthe, E.; Snijders, J. G.; Baerends, E. J. The Zero-Order Regular Approximation for Relativistic Effects: The Effect of Spin−Orbit Coupling in Closed Shell Molecules. *J. Chem. Phys.* **1996**, *105* (15), 6505−6516.
(54) Yates, J. R.; Pickard, C. J.; Mauri, F. Calculation of NMR Chemical Shifts for Extended Systems Using Ultrasoft Pseudopotentials. *Phys. Rev. B* **2007**, *76* (2), No. 024401.
(55) Monkhorst, H. J.; Pack, J. D. Special Points for Brillouin-Zone Integrations. *Phys. Rev. B* **1976**, *13* (12), 5188−5192.
(56) Pfrommer, B. G.; Côté, M.; Louie, S. G.; Cohen, M. L. Relaxation of Crystals with the Quasi-Newton Method. *J. Comput. Phys.* **1997**, *131* (1), 233−240.
(57) Pickard, C. J.; Mauri, F. All-Electron Magnetic Response with Pseudopotentials: NMR Chemical Shifts. *Phys. Rev. B* **2001**, *63* (24), No. 245101.
(58) Oda, K.; Koyama, H. A Refinement of the Crystal Structure of Histidine Hydrochloride Monohydrate. *Acta Crystallogr., Sect. B* **1972**, *28* (2), 639−642.
(59) Pinard, M. A.; Aslan, K. Metal-Assisted and Microwave-Accelerated Evaporative Crystallization. *Cryst. Growth Des.* **2010**, *10* (11), 4706−4709.
(60) Dawson, A.; Allan, D. R.; Belmonte, S. A.; Clark, S. J.; David, W. I. F.; McGregor, P. A.; Parsons, S.; Pulham, C. R.; Sawyer, L. Effect of High Pressure on the Crystal Structures of Polymorphs of Glycine. *Cryst. Growth Des.* **2005**, *5* (4), 1415−1427.
(61) Chandrasekhar, S.; Hota, R.; Choudhury, A. R.T. N. G. R. CCDC 223378: Experimental Crystal Structure Determination *CSD Comm.* 2003 DOI: 10.5517/cc7hfrw.
(62) Strohmeier, M.; Stueber, D.; Grant, D. M. Accurate 13C and 15N Chemical Shift and 14N Quadrupolar Coupling Constant Calculations in Amino Acid Crystals: Zwitterionic, Hydrogen-Bonded Systems. *J. Phys. Chem. A* **2003**, *107* (38), 7629−7642.
(63) Dračínský, M.; Unzueta, P.; Beran, G. J. O. Improving the Accuracy of Solid-State Nuclear Magnetic Resonance Chemical Shift Prediction with a Simple Molecular Correction. *Phys. Chem. Chem. Phys.* **2019**, *21* (27), 14992−15000.
(64) Iuliucci, R. J.; Hartman, J. D.; Beran, G. J. O. Do Models beyond Hybrid Density Functionals Increase the Agreement with Experiment for Predicted NMR Chemical Shifts or Electric Field Gradient Tensors in Organic Solids? *J. Phys. Chem. A* **2023**, *127* (12), 2846−2858.
(65) Ramos, S. A.; Mueller, L. J.; Beran, G. J. O. The Interplay of Density Functional Selection and Crystal Structure for Accurate NMR Chemical Shift Predictions. *Faraday Discuss.* **2025**, *255*, 119−142.
(66) Socha, O.; Hodgkinson, P.; Widdifield, C. M.; Yates, J. R.; Dračínský, M. Exploring Systematic Discrepancies in DFT Calculations of Chlorine Nuclear Quadrupole Couplings. *J. Phys. Chem. A* **2017**, *121* (21), 4103−4113.
(67) Arlin, J. B.; Bhardwaj, R. M.; Johnston, A.; Miller, G. J.; Bardin, J.; Macdougall, F.; Fernandes, P.; Shankland, K.; David, W. I. F.; Florence, A. J. Structure and Stability of Two Polymorphs of Creatine and Its Monohydrate. *CrystEngComm* **2014**, *16* (35), 8197−8204.
(68) Mayo, S. L.; Olafson, B. D.; Goddard, W. A. DREIDING: A Generic Force Field for Molecular Simulations. *J. Phys. Chem. A* **1990**, *94* (26), 8897−8909.
(69) Alderman, D. W.; Sherwood, M. H.; Grant, D. M. Comparing, Modeling, and Assigning Chemical-Shift Tensors in the Cartesian, Irreducible Spherical, and Icosahedral Representations. *J. Magn. Reson., Ser. A* **1993**, *101* (2), 188−197.
(70) Allen, F. H. The Cambridge Structural Database: A Quarter of a Million Crystal Structures and Rising. *Acta Crystallogr., Sect. B* **2002**, *58*, 380−388.
(71) Barr, G.; Dong, W.; Gilmore, C. J.; Kern, A.; Parkin, A.; Wilson, C. C. Using the Cambridge Structural Database to Validate Powder Structures. *Z. Kristallogr.* **2007**, *2007*, 209−214.
(72) Reilly, A. M.; Cooper, R. I.; Adjiman, C. S.; Bhattacharya, S.; Boese, A. D.; Brandenburg, J. G.; Bygrave, P. J.; Bylsma, R.; Campbell, J. E.; Car, R.; Case, D. H.; Groom, C. R.; et al. Report on the Sixth Blind Test of Organic Crystal Structure Prediction Methods. *Acta Crystallogr., Sect. B* **2016**, *72* (4), 439−459.
(73) Hunnisett, L. M.; Francia, N.; Nyman, J.; Abraham, N. S.; Aitipamula, S.; Alkhidir, T.; Almehairbi, M.; Anelli, A.; Anstine, D. M.; Anthony, J. E.; Arnold, J. E.; Cole, J. C.; et al. The Seventh Blind Test of Crystal Structure Prediction: Structure Ranking Methods. *Acta Crystallogr., Sect. B* **2024**, *80* (6), 548−574.
(74) Wang, L.; Harper, J. K. Refining Crystal Structures Using 13C NMR Chemical Shift Tensors as a Target Function. *CrystEngComm* **2021**, *23* (40), 7061−7071.
(75) Toomey, R.; Wang, L.; Heider, E. C.; Hartman, J. D.; Nichols, A. J.; Myles, D. A. A.; Gardberg, A. S.; McIntyre, G. J.; Zeller, M.; Mehta, M. A.; Harper, J. K. NMR-Guided Refinement of Crystal Structures Using 15N Chemical Shift Tensors. *CrystEngComm* **2024**, *26* (25), 3289−3302.
(76) Ishii, Y.; Tycko, R. Sensitivity Enhancement in Solid State 15N NMR by Indirect Detection with High-Speed Magic Angle Spinning. *J. Magn. Reson.* **2000**, *142* (1), 199−204.

(77) Desiraju, G.; Steiner, T. *The Weak Hydrogen Bond*; Oxford University Press: Oxford, England, 2001; Vol. 9 DOI: 10.1093/acprof:oso/9780198509707.001.0001.

https://doi.org/10.1021/acs.molpharmaceut.6c00077
Mol. Pharmaceutics 2026, 23, 3397−3409